Letter

Open Access

Valerio Flavio Gili*, Luca Carletti, Fares Chouchane, Guillaume Wang, Christian Ricolleau, Davide Rocco, Aristide Lemaître, Ivan Favero, Lavinia Ghirardini, Marco Finazzi, Michele Celebrano, Costantino De Angelis and Giuseppe Leo

Role of the substrate in monolithic AlGaAs nonlinear nanoantennas

Abstract: We report the effect of the aluminum oxide substrate on the emission of monolithic AlGaAs-on-insulator nonlinear nanoantennas. By coupling nonlinear optical measurements with electron diffraction and microscopy observations, we find that the oxidation-induced stress causes negligible crystal deformation in the AlGaAs nanostructures and only plays a minor role in the polarization state of the harmonic field. This result highlights the reliability of the wet oxidation of thick AlGaAs optical substrates and further confirms the bulk $\chi^{(2)}$ origin of second harmonic generation at 1.55 μm in these nanoantennas, paving the way for the development of AlGaAs-on-insulator monolithic metasurfaces.

Keywords: harmonic generation and mixing; integrated optics devices; subwavelength structures.

1 Introduction

Dielectric nanophotonics has recently emerged as a very active field due to the strong electric and magnetic
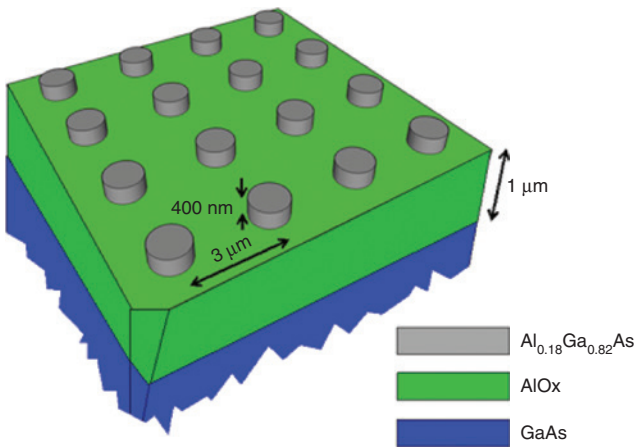
*Corresponding author: Valerio Flavio Gili, Matériaux et Phénomènes Quantiques, Université Paris Diderot – Sorbonne Paris Cité, 10 rue A. Domon et L. Duquet, 75013 Paris, France, e-mail: valerio.gili@univ-paris-diderot.fr
Luca Carletti, Davide Rocco and Costantino De Angelis: Department of Information Engineering, University of Brescia, Via Branze 38, 25123 Brescia, Italy
Fares Chouchane, Guillaume Wang, Christian Ricolleau, Ivan Favero and Giuseppe Leo: Matériaux et Phénomènes Quantiques, Université Paris Diderot – Sorbonne Paris Cité, 10 rue A. Domon et L. Duquet, 75013 Paris, France
Aristide Lemaître: Centre de Nanosciences et de Nanotechnologies, CNRS-UMR9001, Route de Nozay, 91460 Marcoussis, France
Lavinia Ghirardini, Marco Finazzi and Michele Celebrano: Department of Physics, Politecnico di Milano, Piazza Leonardo Da Vinci 32, 20133 Milan, Italy

multipole resonances combined with low losses of metal-less nanoparticles in the visible and near-infrared spectral ranges [1–3]. Semiconductor nanostructures are particularly attractive for on-chip nonlinear optical applications because the electromagnetic field enhancement is not limited to interfaces; thus, higher conversion efficiencies may be achieved compared to plasmonic nanostructures. Although third harmonic generation has been achieved in silicon [4–6] and germanium [7, 8] nanostructures, the central symmetry of these group IV elements forbids bulk second-order nonlinear effects. The latter can be obtained in the optical telecom band with a large-gap III to V optoelectronic material, such as AlGaAs, thanks to its high $\chi^{(2)}$ and negligible linear and two-photon absorption (TPA).

Recently, second harmonic generation (SHG) was demonstrated from high-contrast AlGaAs nanoantennas on low-index insulator substrates [9–12], such as aluminum oxide (AlOx) and transparent benzocyclobutene (BCB). These all-dielectric approaches allowed to considerably boost the SHG efficiency, achieving a nonlinear conversion coefficient $\beta_{SHG} = \hat{P}_{SHG} / \hat{P}_{FW}^2 \cong 6 \times 10^{-6}$ W^{-1}, where $\hat{P}_{SHG}$ and $\hat{P}_{FW}$ indicate the SHG and pump peak powers, respectively. In particular, these systems feature a β_{SHG} that is about 4 orders of magnitude larger than that of especially engineered plasmonic nanostructures, which does not exceed 5×10^{-10} W^{-1} [13]. Moreover, in these nonplasmonic nanoantennas, the SHG signal was shown to be driven by a magnetic dipole resonance at the fundamental frequency [9], leading to a higher-order multipole mode at 2ω with a very rich polarization behavior [14]. To appreciate the role of the substrate in the above achievements, let us recall that 10^{-3} SHG efficiency is expected for an idealized Al$_{0.18}$Ga$_{0.82}$As nanocylinder surrounded by air, for an incident intensity $I_0 = 1$ GW/cm^2 at 1.55 μm [15]. For the same nanoantenna on an AlOx substrate ($n \approx 1.6$), with $I_0 = 1.6$ GW/cm^2, the corresponding SHG efficiency drops to 1.1×10^{-5} [9], whereas, in the case of AlGaAs-on-BCB (n ≈ 1.35), an efficiency of 8.5×10^{-5} has been shown for an incident power of 7 GW/cm^2 [12]. More recently, a 2×10^{-6} SHG conversion efficiency has been observed in GaP-on-GaP nanoantennas

Figure 1: Schematic view of the AlGaAs-on-AlOx nanocylinder array.

for an incident power of 200 GW/cm^2 [16], dramatically highlighting the importance of a low-refractive-index substrate in nonlinear nanophotonics applications.

In the case of AlGaAs-on-AlOx nanoantennas, the oxidation process of such a substrate could in principle produce mechanical stress in the nanocylinder. This effect was recently exploited to achieve controlled deformation of the nonlinear susceptibility tensor [17, 18]. This motivates a detailed study on the role of the substrate in the AlGaAs-on-AlOx platform, with particular attention to fabrication tolerances and their effect on SHG measurements. Hereafter, based on transmission electron microscopy (TEM) and electron diffraction imaging, we exclude that oxidation-induced stress can modify the $\chi^{(2)}$ tensor of the nanostructures and only results in a slight change of the SHG polarization. These results confirm the robustness of our monolithic fabrication technique and strengthen the claim that SHG in our nanostructures is purely due to bulk $\chi^{(2)}$ [14].

2 Fabrication and experiments

Our samples were fabricated on a (100) nonintentionally doped GaAs wafer, with a 400 nm layer of $Al_{0.18}Ga_{0.82}As$ on top of an aluminum-rich substrate. We first used electron beam lithography to pattern a rectangular array of circles with nominal radii varying from 175 to 225 nm along the [110] direction and e-beam dose varying from 108 to 228 μC/cm^2 along the [1$\bar{1}$0] direction followed by ICP-RIE dry etching with $SiCl_4$. Lastly, we performed a selective oxidation of the Al-rich substrate with an H_2:N_2 gas carrier at 390°C for 30 min. The result is an array of nanocylinders with variable radius, equally spaced by 3 μm, as sketched in Figure 1.

To experimentally probe the nonlinear properties of AlGaAs nanoantennas, we employed the setup described in Ref. [9], which consists of a confocal microscope coupled with a linearly polarized (extinction ratio >100:1) ultrafast laser (150 fs pulse width) centered at 1.55 μm. To access the various multipole resonances at the SH frequency and gain spectral information without varying the excitation wavelength, we analyzed nanoantennas with different radii [12]. Figure 2A reports the SHG intensity map on a portion of the array of AlGaAs nanoantennas, with variable nominal radius (192–203 nm) and e-beam dose. Extracting the data from the second row, we plotted in Figure 2B the SHG intensity counts as a function of position, finding a signal-to-noise ratio of more than 10^4 [9].

Figure 3 shows the experimental polar plots retrieved from a series of SHG confocal maps on individual, virtually identical nanoantennas located in six different arrays fabricated using identical parameters. The measurements show different tilt angles ranging from −9° to 6° in the SHG radiation diagram for each nanocylinder.
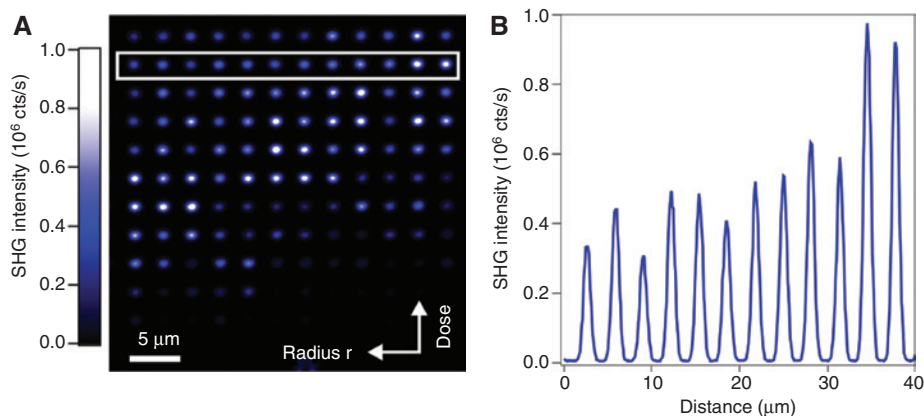
Figure 2: The nanodisks separation is about 3 micron, which sufficient to allow single-particle nonlinear microscopy. The SHG detection with silicon SPAD allows achieving a signal-to-noise ratio exceeding 10^4.
(A) SHG intensity map of an array of nanodisks with radius varying from 192 to 203 nm (from right to left) and increasing electron-beam lithography dose (from bottom to top). (B) Line profile of the SHG intensity along the second row of the array (see white box in A).
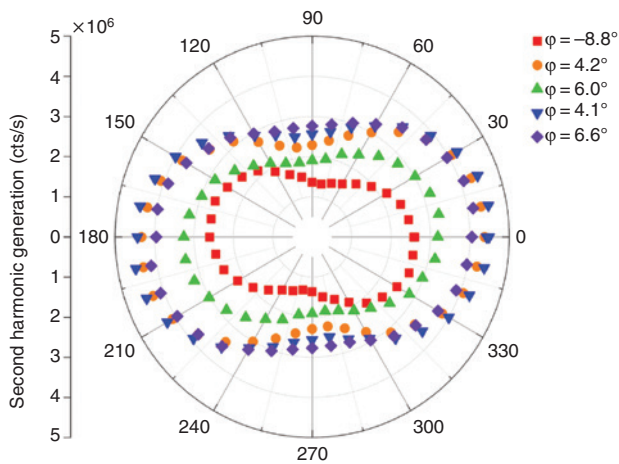
Figure 3: SHG polar plots of virtually identical nanoantennas. The tilt angle φ ranges from −8.8° to 6.6°.

Very recently, the analysis of SHG polarization properties in the same nanoantennas showed its pure bulk $\chi^{(2)}$ origin [14] as opposed to the hypothesis of surface

$\chi^{(2)}$ contribution in GaAs nanoantennas affected by TPA [10]. To understand if the observed tilts in the radiation diagrams can be explained by a lattice deformation in AlGaAs pillars resulting in off-diagonal terms in the $\chi^{(2)}$ tensor, TEM and electron diffraction characterization of our nanostructures were combined with finite-element simulations.

Before TEM observation, a platinum layer was deposited on the sample for metallization, and a cross-section thin film was extracted from the whole sample using Zeiss crossbeam Ga focused ion beam (FIB). The plane of this thin film is (001) and contains three virtually identical pillars, with their axis nominally oriented perpendicular to the [110] direction, as sketched in Figure 4A. We performed TEM analysis on a JEOL ARM 200F electron microscope equipped with a spherical aberration corrector. High-resolution TEM images show that the three AlGaAs pillars are single crystals without any alteration of the crystalline matrix (see Figure 4B and C). However, according to electron diffraction experiments on selected areas, their crystallographic directions are neither strictly
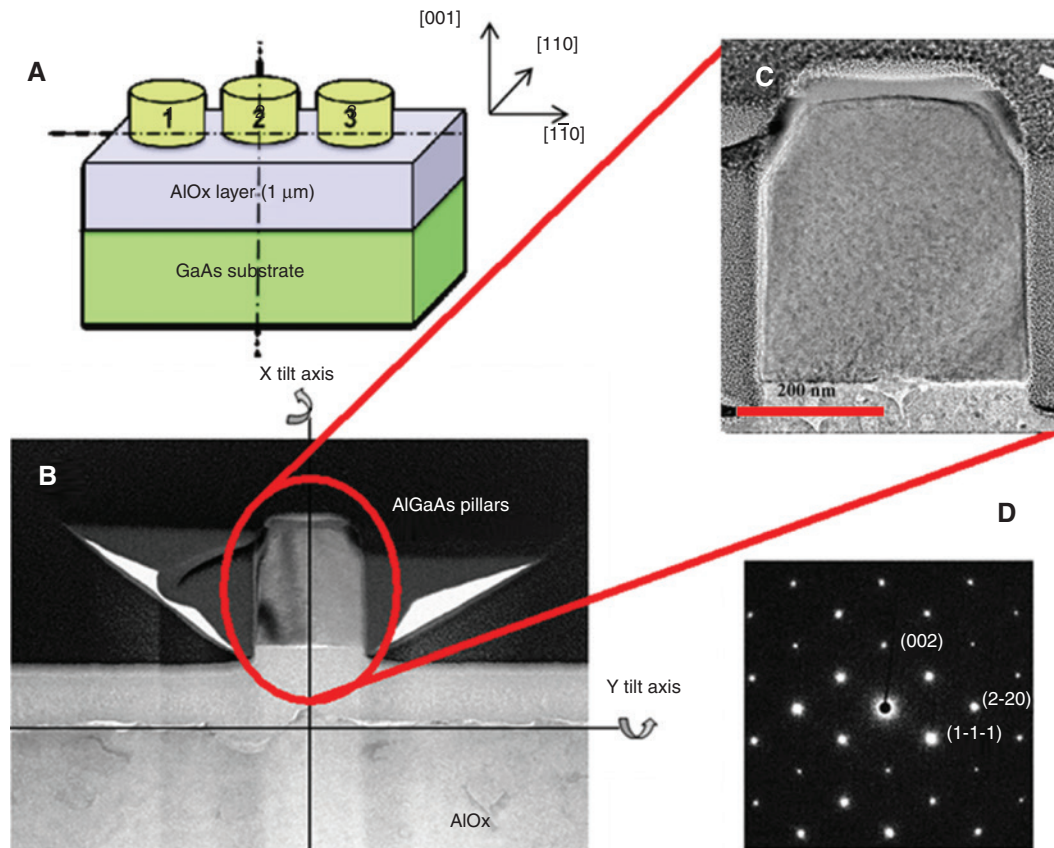
Figure 4: (A) Scheme of the sample for TEM prepared by FIB and (B) TEM picture of AlGaAs/AlOx nanoantenna 2, with indications of the crystalline rotations around the [001] (*X*) and [1$\bar{1}$0] (*Y*) axes.
The brighter area is the AlOx layer, whereas the darker area surrounding the pillar is platinum. (C) High-resolution detail of Figure 4B and (D) electron diffraction pattern of nanoantenna 2.

parallel to the ones of the GaAs substrate nor to each other, showing a tilt around the vertical (*X*) and horizontal (*Y*) axes.

Using a double-tilt sample holder, we determined the rotation angles of the three nanoantennas with respect to the [001] (*X*) and [1̄10] (*Y*) directions by comparing their electron diffraction maps (Figure 4D, the one of pillar 2) to the one of the GaAs substrate. It appears that the AlGaAs pillars have lost their epitaxial relationship with the GaAs wafer due to the presence of the AlOx amorphous layer. The measured rotations around the *X* axis with respect to the substrate are $\theta \approx 5.5°$, 2.9°, and 0.5° for nanoantennas 1, 2, and 3, respectively, whereas the rotations around the *Y* axis are less significant.

3 Modeling and discussion

To gain further insight in our experimental results, we performed finite-element numerical simulations with COMSOL Multiphysics. As the oxidation of the Al-rich layer induces a substantial volume shrinkage of 10%–13%, which in principle might lead to a significant strain in the proximity of the AlOx [17, 18], we dedicated a first part of our numerical analysis to the evaluation of the mechanical strain distribution in the nanoantennas and its possible effect on SHG. $Al_xGa_{1-x}As$ was considered as an anisotropic material with the following mechanical properties: poisson's coefficient $v = 0.31 + 0.1x$ and elasticity tensor components $C_{11} = (118.8 + 1.4x)$ GPa, $C_{12} = (53.8 + 3.2x)$ GPa, and $C_{44} = (59.4 - 0.5x)$ GPa [19]. As AlOx is amorphous and not stoichiometric, its exact mechanical properties are unknown. As an approximation, we used γ-Al_2O_3 parameters (Young modulus: $E = 400$ GPa, $v = 0.21$) [20]. We have considered an elastic strain of 13% in the oxide layer along the direction perpendicular to the substrate plane. As shown in Figure 5, the strain in the nanodisks seems to be extremely low ($<10^{-3}$) compared to the values employed for SHG enhancement in silicon [17, 18] and is mainly located in the immediate vicinity of the AlOx/AlGaAs interface. From these numerical results, along with TEM observations, we can assert that no significant deformation of the $\chi^{(2)}$ tensor occurs.

Finally, we performed fully vectorial frequency-domain finite-element calculations to assess the impact of the crystalline rotation on the tilt of the SH polar plots from single nanoantennas. We model this stress-induced rotation of the principal axes by defining an angle θ between the [110] crystalline axis and the linearly polarized electric field of the pump impinging at normal incidence on a stress-free nanoantenna, as shown in Figure 6 (inset). For
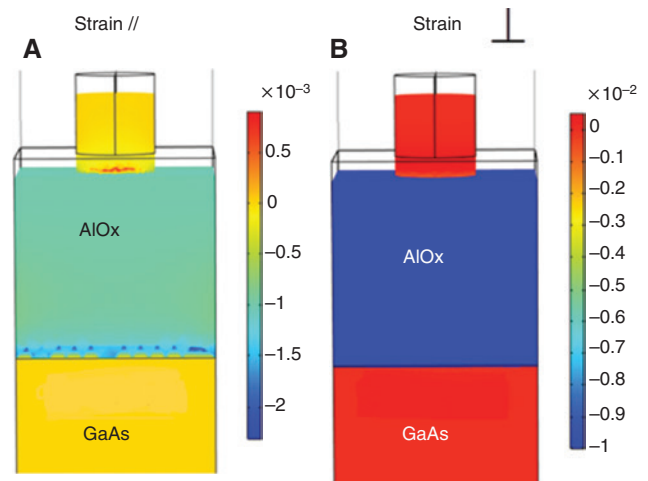
Figure 5: Finite-element map of the oxidation-induced strain on the nanoantenna parallel (A) and perpendicular (B) to the wafer plane. The latter is zero, whereas the former is much lower than the typical values that induce a nonvanishing $\chi^{(2)}$ in silicon.
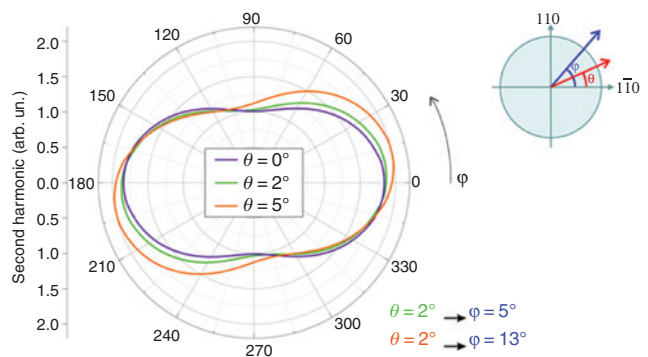
Figure 6: Calculated polarization plots of the emitted SH for a few values of θ (with θ and φ defined in the inset).
The range of the estimated values of φ is compatible with the SHG experimental polar plot of Figure 3.

definition, θ is thus completely equivalent to the tilt angle around the *X* axis, measured with electron diffraction (see Figure 4D). We inferred its impact on the angle φ between the prevailing SH linear polarization and the [1̄10] axis by calculating polarization plots of the emitted SH shown in Figure 6. From these results, we can conclude that the values of θ consistent with electron diffraction measurements (2–5°) give rise to a range of values for φ (5–13°) that are in good agreement with the SHG measurements.

4 Conclusion

We have assessed the limitations of the AlOx substrate on the SHG in AlGaAs-on-insulator monolithic nanoantennas.

We found in both simulations and TEM observations that the mechanical stress induced during the oxidation procedure does not extend to the whole nanoantenna, leaving the nonlinear susceptibility tensor basically unaltered. On the contrary, electron diffraction showed a rotation in the (001) plane, in agreement with both measured and simulated SH radiation diagrams.

References

[1] Kuznetsov AI, Miroshnichenko AE, Fu YH, Zhang J, Luk'yanchuk B. Magnetic light. Sci Rep 2012;2:1–6.

[2] Evlyukhin AB, Novikov SM, Zywietz U, et al. Demonstration of magnetic dipole resonances of dielectric nanospheres in the visible region. Nano Lett 2012;12:3749–55.

[3] Person S, Jain M, Lapin Z, Sáenz JJ, Wicks G, Novotny L. Demonstration of zero optical backscattering from single nanoparticles. Nano Lett 2013;13:1806–9.

[4] Shcherbakov MR, Neshev DN, Hopkins B, et al. Enhanced third-harmonic generation in silicon nanoparticles driven by magnetic response. Nano Lett 2014;14:6488–92.

[5] Shcherbakov MR, Shorokhov AS, Neshev DN, et al. Nonlinear interference and tailorable third-harmonic generation from dielectric oligomers. ACS Photon 2015;2:578.

[6] Yang Y, Wang W, Boulesbaa A, et al. Nonlinear fano-resonant dielectric metasurfaces. Nano Lett 2015;15:7388–93.

[7] Grinblat G, Li Y, Nielsen MP, Oulton RF, Maier SA. Enhanced third harmonic generation in single germanium nanodisks excited at the anapole mode. Nano Lett 2016;16:4635–40.

[8] Celebrano M, Baselli M, Bollani M, et al. Emission engineering in germanium nanoresonators. ACS Photon 2015;2:53.

[9] Gili VF, Carletti L, Locatelli A, et al. Monolithic AlGaAs second-harmonic nanoantennas. Opt Express 2016;24:15965.

[10] Liu S, Sinclair MB, Saravi S, et al. Resonantly enhanced second-harmonic generation using III-V semiconductor all-dielectric metasurfaces. Nano Lett 2016;16:5426–32.

[11] Camacho R, Rahmani M, Kruk S, et al. Nonlinear generation of vector beams from AlGaAs nanoantennas. Nano Lett 2016;16:7191–7.

[12] Carletti L, Rocco D, Locatelli A, et al. Controlling second-harmonic generation at the nanoscale with monolithic AlGaAs-on-AlOx antennas. Nanotechnology 2017;28:114005.

[13] Kauranen M, Zayats AV. Nonlinear plasmonics. Nat Photon 2012;6:737–48.

[14] Ghirardini L, Carletti L, Gili G, et al. Polarization properties of second-harmonic generation in AlGaAs optical nanoantennas. Opt Lett 2017;42:559–62.

[15] Carletti L, Locatelli A, Stepanenko O, Leo G, De Angelis C. Enhanced second-harmonic generation from magnetic resonance in AlGaAs nanoantennas. Opt Express 2015;23:26544–50.

[16] Cambiasso J, Grinblat G, Li Y, Rakovich A, Cortés E, Maier SA. Bridging the gap between dielectric nanophotonics and the visible regime with effectively lossless gallium phosphide antennas. Nano Lett 2017;17:1219–25.

[17] Cazzanelli M, Bianco F, Borga E, et al. Second-harmonic generation in silicon waveguides strained by silicon nitride. Nat Mater 2012;11:148–54.

[18] Schriever C, Bianco F, Cazzanelli M, et al. Second-order optical nonlinearity in silicon waveguides: Inhomogeneous stress and interfaces. Adv Opt Mater 2015;3:129–136.

[19] Adachi S. GaAs and related materials: bulk semiconducting and superlattice properties. World Scientific, 1994.

[20] Chouchane F, Almuneau G, Cherkashin N, Arnoult A, Lacoste G, Fontaine C. Local stress-induced effects on AlGaAs/AlOx oxidation front shape. Appl Phys Lett 2014;105:041909.